frontiers | Frontiers in Nuclear Engineering

TYPE Original Research
PUBLISHED 12 November 2024
DOI 10.3389/fnuen.2024.1486694

OPEN ACCESS

EDITED BY
Xiaofeng Guo,
Washington State University, United States

REVIEWED BY
Sourabh Bhagwan Kadambi,
Idaho National Laboratory (DOE), United States
Devanshi Bhardwaj,
Stony Brook University, United States

*CORRESPONDENCE
Alice Perrin,
perrinae@ornl.gov

RECEIVED 26 August 2024
ACCEPTED 14 October 2024
PUBLISHED 12 November 2024

CITATION
Perrin A, Hamaguchi D, Geringer JW, Zinkle S, Yang Y, Skutnik S, Poplawsky J and Katoh Y (2024) Microstructure, electrical resistivity, and tensile properties of neutron-irradiated Cu–Cr–Nb–Zr.
Front. Nucl. Eng. 3:1486694.
doi: 10.3389/fnuen.2024.1486694

Microstructure, electrical resistivity, and tensile properties of neutron-irradiated Cu–Cr–Nb–Zr

Alice Perrin[1]*, Dai Hamaguchi[2], Josina W. Geringer[1], Steve Zinkle[1,3], Ying Yang[1], Steve Skutnik[4], Jon Poplawsky[1] and Yutai Katoh[1]

[1]Materials Science and Technology Division, Oak Ridge National Laboratory, Oak Ridge, TN, United States, [2]National Institutes for Quantum Science and Technology, Fusion Energy Directorate, Rokkasho Fusion Institute, Chiba, Japan, [3]Department of Nuclear Engineering, University of Tennessee, Knoxville, TN, United States, [4]Nuclear Energy and Fuel Cycle Division, Oak Ridge National Laboratory, Oak Ridge, TN, United States

High strength, high conductivity copper alloys that can resist creep at high temperatures are one of the primary candidates for efficient heat exchangers in fusion reactors. Cu–Cr–Nb–Zr (CCNZ) alloys, which were designed to improve the strength and creep life of ITER Cu–Cr–Zr (CCZ) reference alloys, have been found to have comparable electrical conductivity and tensile properties to CCZ alloys. The measured creep rupture times for these improved alloys is about ten times higher than the ITER reference alloys at 90–125 MPa at 500 °C. However, the effects of neutron irradiation on these alloys, and the ensuing material properties, have not been studied; thus, their utility in a fusion reactor environment is not well understood. This study characterizes the room temperature mechanical and electrical properties of a neutron-irradiated CCNZ alloy and compares them to a neutron-irradiated ITER reference heat sink CCZ alloy. Tensile specimens were neutron irradiated in the High Flux Isotope Reactor (HFIR) to 5 dpa between 250 °C and 325 °C. Post-irradiation characterization included electrical resistivity measurements, hardness, and tensile tests. Microstructural evaluation used scanning electron microscopy, energy dispersive x-ray spectroscopy, and atom probe tomography to characterize the irradiation-produced changes in the microstructure and investigate the mechanistic processes leading to post-irradiation properties. Transmutation calculations were validated with composition measurements from atom probe data and used to calculate contributions to the increased electrical resistivity measured after irradiation. Comparisons with CCZ alloys in the same irradiation heat found that the post-irradiated CCNZ and CCZ alloys had comparable electrical resistivity. Although CCNZ alloys suffered more irradiation hardening than CCZ, the overall tensile behavior deviated very little from non-irradiated values in the temperature range studied.

KEYWORDS

conductivity, Cu alloy, CCNZ, heat exchanger, tensile properties, neutron irradiation

1 Introduction

Divertors of impurities and helium ash from burning plasma in fusion reactors are one of the components in nuclear fusion reactors that experience extremely high heat fluxes (You et al., 2021). In addition to high-melting-point plasma facing components (PFCs), divertors require high-strength, creep-resistant, high thermal conductivity materials to efficiently draw heat from PFCs (Asakura et al., 2023). The International Thermonuclear Experimental Reactor (ITER) is a scientific research reactor currently under construction in France which is intended to achieve burning plasma, test the safety and functionality of integrated fusion power plant designs, and demonstrate the generation of fusion power at levels ten times the input heating power needed to sustain plasma (Siccinio et al., 2020; ITER Organization, 2024). The European demonstration power plant, EU-DEMO, is ITER's planned successor and will be a larger reactor intended to produce a net electrical power output (×25 input) on a continuous basis (EUROfusion, 2024). EU-DEMO will use and build upon knowledge gained from ITER, but its larger size and broader power generation goals require materials with operational limits significantly higher than required for ITER operation. High heat flux materials for divertors may face an order of magnitude greater total radiation damage, an estimated 6–13 dpa greater in EU-DEMO than in ITER, (You et al., 2021) and experience temperatures 300–400 °C (Zinkle and Ghoniem, 2000; Zinkle, 2016).

The high electrical conductivity (and thus high thermal conductivity, due to the Wiedemann–Franz law) of Cu makes it attractive for high heat flux components; however, pure Cu lacks the mechanical properties needed in high temperature reactor conditions. Alloys such as GlidCop Al25 (Fabritsiev and Pokrovsky, 2007), GRCop-84 (Groh et al., 2008), CuNiBe (Zinkle, 2014), Cu–Al_2O_3, and CuCrNiSi (Wang et al., 2015) have been developed in the hopes of producing stronger alloys without degradation of the thermal conductivity. Cu–Cr–Zr (CCZ) alloys have been identified as a promising candidate for commercial reactor heat exchange components. CCZ was selected for use in the divertors, first wall, and blanket components of the ITER fusion facility (Barabash et al., 2007) due to its relatively high thermal conductivity and good mechanical properties up to 300 °C, with an ultimate tensile strength of 325 MPa at 300 °C in peak aged condition (Edwards et al., 2007). Although CCZ has been studied and developed based on ITER specifications (Barabash et al., 2011; Gusarov et al., 2018; Fabritsiev and Pokrovsky, 2005), the greater dose and temperature demands of the DEMO reactor are beyond the optimal operating limits achieved with ternary CCZ alloys (Zinkle, 2016). In particular, based on limited testing, the creep strength of CCZ falls rapidly with increasing temperatures above 300 °C, with the design allowable stress for ITER-grade CCZ falling below 50 MPa at temperatures above ~360 °C due to thermal creep. (Asakura et al., 2023; Terentyev et al., 2023; Zinkle and Ghoniem, 2000; Zinkle, 2016; Zinkle and Fabritsiev, 1994; Barabash et al., 2011; You, 2015; Groh et al., 2008).

New Cu–Cr–Nb–Zr (CCNZ) alloys were designed to improve the strength and creep life of CCZ alloys by combining the fine precipitate strengthening of CCZ with the Laves phase strengthening of Cu–Cr–Nb (GRCop-84) alloys (Yang et al., 2018; Wang et al., 2020; Cheng et al., 2021; Krishna et al., 2022; Anderson et al., 1995; Groh et al., 2008). This was achieved through a bimodal distribution of precipitates with coarse Cr_2(Nb,Zr) Laves phase precipitates at grain boundaries (GB) as well as nanoscale Cr and Cu_5Zr nanoprecipitates in the matrix. The Cr_2(Nb,Zr) GB precipitates can effectively pin grain boundaries and mitigate grain boundary sliding-induced creep. The measured creep rupture times for these improved CCNZ alloys is about ten times higher than the ITER reference CCZ alloys at 90–125 MPa at 500 °C (Gusarov et al., 2018; Wang et al., 2020). The tensile properties and electrical conductivity of the advanced CCNZ and ITER CCZ alloys are comparable. However, despite the need for a clear understanding of the neutron irradiation effects on alloys designed for use in cooling channels of ITER and DEMO divertors, only limited information is available on these material properties (Barabash et al., 2011; Kalinin et al., 2011; Li and Zinkle, 2020).

Given this knowledge gap, this study focuses on the room temperature electrical and mechanical properties of neutron irradiated CCNZ alloys and compares them to CCZ alloys irradiated under the same conditions. Through subsequent microstructural evaluation and transmutation calculations, we correlated this data with the various radiation-induced changes in these alloys.

2 Experimental methods

Cu alloys with a nominal composition of Cu-2Cr-1.35Nb-0.15Zr (wt%) were arc-melted from pre-alloyed bulk Cu-21.3wt%Nb, Cr, and Zr and drop cast to form bars. The cast bars were subjected to multiple passes of cold rolling followed by high temperature (970 °C) solution annealing and subsequent thermal aging at 475 °C for 3 h, resulting in a microstructure containing a high density of nanoscale Cr precipitates and larger Cr_2Nb precipitates. The detailed experimental procedure for Cu alloy casting and processing was described in detail by Yang et al. (2018) and Wang et al. (2020). ITER-grade CCZ specimens with a nominal composition of Cu-0.81Cr-0.07Zr were fabricated in a similar process, with a cold rolled sample solution annealed at 980 °C before thermal aging at 475 °C for 3 h to precipitate nanoscale Cr precipitates. Wire electrical discharge machining (EDM) was used to cut samples into SSJ3 tensile specimens. CCNZ and CCZ specimens were irradiated for three cycles in the HFIR flux trap facility to target a damage dose of 5dpa (based on the stainless steel equivalent) and irradiation temperatures (T_{ir}) of 250–350°C. It completed up to ~6454 MWD (at nominal operating power of 85W) and was exposed to a total fast fluence of 6.8–7.6 ($\times 10^{25}$) n/m^2 for E > 0.1 MeV. This resulted in displacement damage of 7.8e14 n/cm$^{2\text{-}s}$ (E > 0.1 MeV), which is roughly 7.2e-7 dpa/s in Cu, assuming E_d = 30 eV. The corresponding thermal neutron flux is 2.2e15 n/cm$^{2\text{-}s}$. The actual temperatures were between 241 °C and 359 °C. Exact irradiations temperatures of specimens were derived from a combination of SiC thermometry placed around specimens in each capsule and finite element analysis of capsule heat flow; experimental irradiation temperatures can be found in Table 1 (Howard and Smith, 2018; Field et al., 2019; Campbell et al., 2016).

We studied six tensile specimens of CCNZ. Since thermometry and finite element analysis calculations revealed that the irradiation temperatures of each specimen were fairly evenly spaced at intervals

TABLE 1 Measured irradiation temperatures, resistivity, hardness, and tensile properties for CCNZ.

Irradiation temperature T_{ir} (°C)	Electrical resistivity (μΩ*cm)	Electrical conductivity (%IACS)	Average hardness (HV)	Yield strength (YS) (MPa)	Ultimate tensile strength (UTS) (MPa)	Uniform elongation (UE) (%)	Total elongation (TE) (%)
254	4.37	39.38	161 ± 5	358	449	9.8	16.3
268	4.47	38.53	158 ± 4	334	441	13.7	20.3
280	3.81	45.22	155 ± 5	258	463	16.3	22.6
294	3.70	46.51	149 ± 2	318	419	12.4	18.7
304	3.93	43.77	147 ± 7	336	450	12.8	17.4
318	4.10	41.95	150 ± 4	428	436	3.8	10.5

of 10–14 °C, each specimen was considered a unique data point; arbitrarily grouping the points would obscure some of the temperature-dependent trends observed in this study. Post-irradiation experiments were performed primarily in the Low Activation Materials Development and Analysis Laboratory (LAMDA) at Oak Ridge National Laboratory. The examination of a limited number of ITER-grade CCZ samples was also performed in order to obtain reference comparison points. Electrical resistivity measurements were performed with a custom built system for performing four-point measurements (Echols et al., 2023). Resistivity was measured across the area of each tensile specimen gauge (5 mm × 1.2 mm, 0.75 mm thick). Five readings of voltage and current were taken for each specimen after 5 s and averaged; a measure of the voltage and current after a 30 s hold was also taken for each sample. Vickers hardness measurements were taken at room temperature with a Buehler Tukon 3100. Each indentation had an applied load of 500 gf and a dwell time of 15 s; the reported hardness for each specimen was the average of five indentations. Tensile testing was performed at room temperature with an MTS Insight Electromechanical Test Frame at a constant strain rate of 10^{-3} 1/s; standard deviations are not available for this data as only one specimen was available for each irradiation temperature. Experimentally measured resistivity, hardness, and tensile testing data points for each sample can be found in Table 1.

Microstructural characterization consisted of scanning electron microscopy (SEM) and atom probe tomography (APT). Samples were polished for SEM with colloidal silica down to a final polish of 0.5 μm. SEM imaging was performed with a TESCAN MIRA3 GMH microscope in backscatter electron detection (BSE) mode at 10 kV, and energy dispersive X-ray spectroscopy (EDS) was used to identify phases and estimate compositions in the Laves phase and Cu matrix. ImageJ was used to analyze microstructural feature sizes and thresholding of void area fractions. APT nanotips were prepared using a dual-beam FEI Versa 3D focused ion beam (FIB). A Cameca Instruments LEAP4000X HR tomograph was used to analyze APT tips in laser mode at the Center for Nanoscale Materials Science (CNMS) at ORNL. A detailed description of the APT tip preparation and characterization process can be found in Bahl et al. (2021). Although tensile, hardness, and resistivity data were obtained for all samples, SEM was limited to three samples at varying irradiation temperatures. APT analysis was limited to one specimen, the sample with T_{ir} = 318 °C, due to the time-intensive nature of radioactive sample preparation for both techniques.

Transmutation products were calculated using ORIGEN, part of the SCALE code system (Wieselquist and Lefebvre, 2023). One-group transition coefficients used by ORIGEN were calculated using a 252-group HFIR spectrum for the flux trap regions (Xoubi and Primm, 2004). This model has been previously validated against historic flux wire activation data to confirm its accuracy (Skutnik and Austin, 2023). Based on the sample positions relative to the reactor midplane within the flux trap region, the total effective flux for each sample as adjusted per the empirical fit functions was derived from historic flux wire activation data, assuming a nominal midplane scalar flux of 3.98 $*10^{15}$ n/cm^2·s (*ibid*). In general, flux corrections for the axial locations of the samples were less than 4% of the nominal flux. Depletion modeling assumed that the reactor was at full nominal (85 MW) power over the entirety of each irradiation interval, with inter-cycle outages explicitly accounted for.

3 Results

3.1 Hardness and tensile measurements

Hardness testing found irradiation hardening in CCNZ, which decreased with increasing irradiation temperature up to 300 °C, at which point a slight upturn was observed, mimicking trends observed in CCZ for the same irradiation conditions (Figure 1; Table 1). Compared to the non-irradiated hardness of 119 HV, the maximum irradiation hardening was observed for the sample irradiated at 254 °C, with an average hardness of 161 HV (an increase of 36%). Irradiation hardening was lowest in the samples irradiated at 304–318 °C, which had an average hardness of 147 HV (an increase of 23% from the non-irradiated alloy). Tensile testing found that CCNZ alloys generally maintained their advantageous ultimate tensile strength (UTS) over CCZ at room temperature even at high irradiation temperatures (Figure 2A), and the UTS for both alloys did not deviate more than 6% from their non-irradiated values. Greater variation was observed in both the yield strength (YS) and elongation data for CCNZ (Figures 2A, C).

Yield strength, uniform elongation (UE), and total elongation (TE) generally showed a weak variation with temperature (Figure 2). CCNZ's YS generally exhibited a slight decrease with increasing irradiation temperature (except for a relatively low value at 280 °C and a relatively high value at 320 °C—Figure 2B). The irradiated

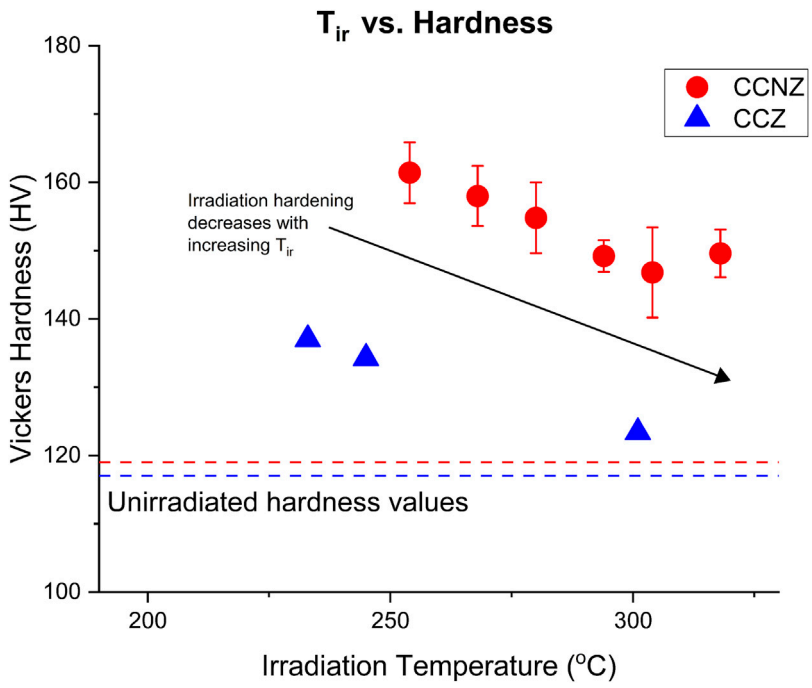

FIGURE 1
Room temperature micro-hardness as a function of irradiation temperature.

CCNZ UTS values did not exhibit any statistically significant variation compared to the unirradiated value over the irradiation temperature range investigated. The irradiated CCNZ uniform and total elongation were lower than the unirradiated values at ~ 250 °C and ~320 °C. In comparison, the YS for irradiated CCZ exhibited slightly more pronounced (~10%) irradiation hardening than the CCNZ samples, although the limited amount of CCZ data prohibited more in-depth trend analysis (Figures 2B, D).

3.2 Electrical resistivity

Electrical resistivity measurements (Figure 3A) and the corresponding electrical conductivity values of the irradiated samples (Figure 3B) are summarized in Figure 3. For materials such as Cu alloys, where electron-phonon collisions dominate the electron transport, electrical conductivity (σ) is proportional to thermal conductivity (k_{th}) as designated by the Wiedemann–Franz law, $k_{th}/\sigma = LT$, where T is absolute temperature and L is the Lorenz number (ideally equal to 2.44×10^{-8} V^2/K^2). Heat transfer occurs through both electron and phonon movement, but the large concentration of free electrons controlling electrical conductivity also allows them to dominate heat transport in metals. Thus, the more easily measured electrical resistivity provides an accurate estimate of the degradation of the thermal conductivity of CCNZ under irradiation. The electrical conductivity was calculated from the experimental electrical resistivity, ρ:

$$\rho = \frac{V}{I}*\frac{A}{l}, \quad (1)$$

where V = voltage, I = current, l = length of the specimen between electrical contacts, and A = cross sectional area between electrical contacts. Conductivity, σ, is often reported in units of % of the International Annealed Copper Standard (IACS), where 100% IACS = $5.8*10^7$ S/m, the reference conductivity of annealed copper. To calculate σ in units of % IACS from the experimentally determined ρ values (Equation 1), the relationship between the values is

$$\sigma = \frac{1}{\rho}*\frac{(100\%)}{5.8*10^7\ S/m} = \frac{1.72*10^{-6}}{\rho}\ \%, \quad (2)$$

where ρ is reported in SI units of Ω-m. Although non-irradiated CCNZ has lower electrical conductivity than CCZ (84% vs. 72% IACS, per Equation 2) (Wang et al., 2020), both alloys after irradiation have comparable conductivity (Figure 3B). The post irradiation conductivity, $\sigma_{T_{ir}=300℃}$, of CCNZ irradiated approximately 300 °C was 43.8% IACS (Figure 3B; Table 1), a 39% decrease in conductivity from non-irradiated CCNZ. $\sigma_{T_{ir}=300℃}$ = 45.5% IACS for CCZ, constituting a 39% decrease in conductivity compared to its non-irradiated counterpart. For samples irradiated at 254 °C, a somewhat lower conductivity was observed in the CCNZ alloys: $\sigma_{T_{ir}=250℃}$ = 39.3%IACS ($\Delta\sigma$ = −45.4%), while the CCZ alloy's $\sigma_{T_{ir}=250℃}$ = 45.1%IACS ($\Delta\sigma$ = −39.7%). These values correspond to resistivities of $\rho_{CCZ} = 3.78\mu\Omega \cdot cm$ ($\Delta\rho_{CCZ} = 1.73\mu\Omega \cdot cm$), $\rho_{CCNZ} = 3.92\mu\Omega \cdot cm$ ($\Delta\rho_{CCNZ} = 1.55\mu\Omega \cdot cm$). The non-linear CCNZ electrical resistivity data versus irradiation temperature suggests competition of multiple temperature-dependent contributions to the resistivity change, producing an inflection point in the data between 270 °C and 280 °C.

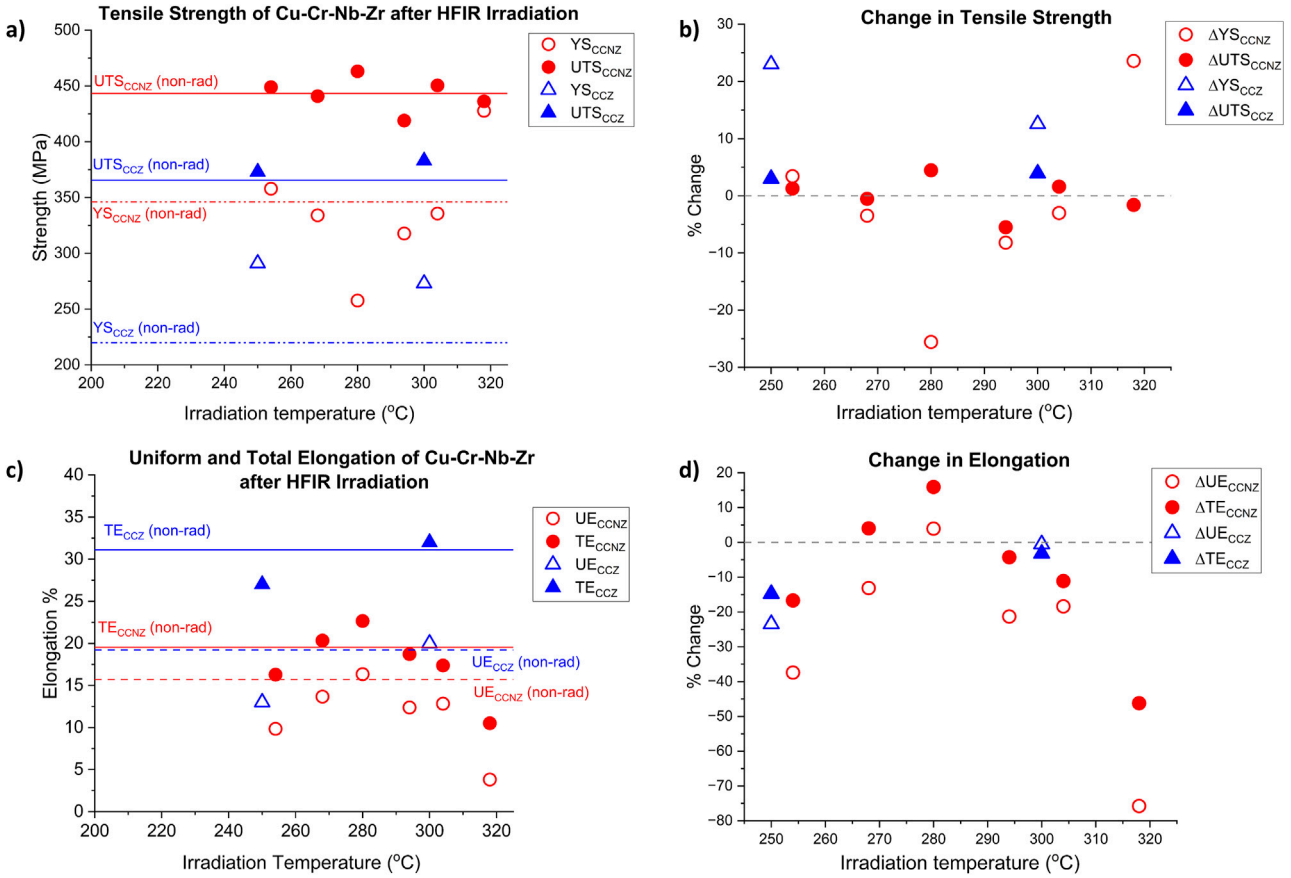

FIGURE 2
(A) Yield (YS) and ultimate tensile strength (UTS) of CCNZ before and after irradiation compared with ITER-grade CCZ (tested at room temperature). **(B)** Percentage change in tensile strength versus irradiation temperature. **(C)** Uniform (UE) and total (TE) elongation of CCNZ before and after irradiation compared to ITER-grade CCZ. **(D)** Percentage change in elongation versus irradiation temperature.

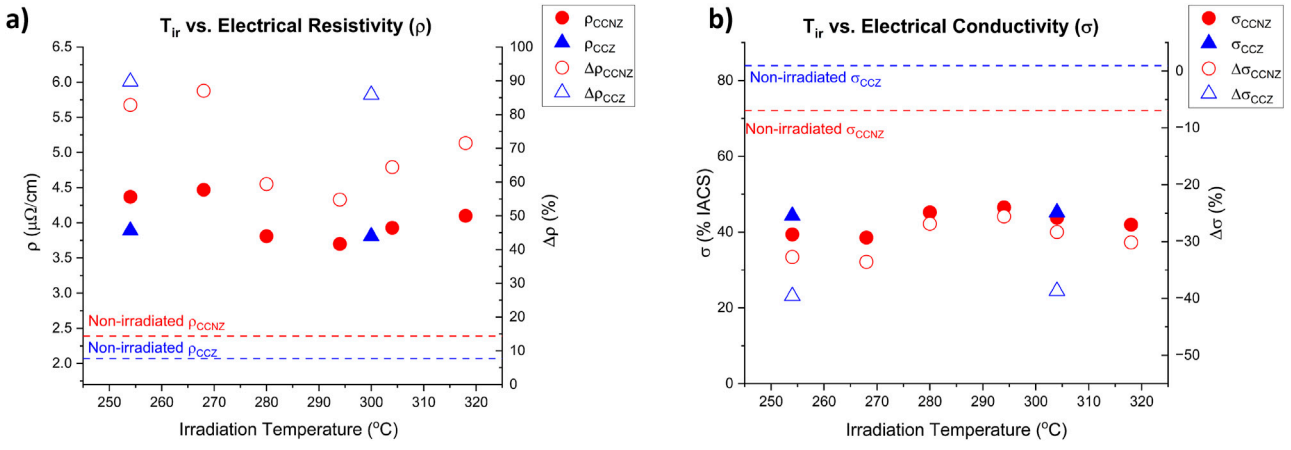

FIGURE 3
(A) Electrical resistivity (ρ) of CCNZ after irradiation compared with irradiated CCZ in identical irradiation conditions (filled markers); non-irradiated values are shown with dotted lines. Open markers show the change in resistivity from non-irradiated values. **(B)** Calculated electrical conductivity (σ) of CCNZ and CCZ (filled markers) from data in **(A)** along with the change in conductivity from non-irradiated specimens (open markers).

TABLE 2 Transmutation calculations for CCNZ and ITER-grade CCZ at T_{ir} = 300 °C showing estimated post-irradiation compositions, the isotopes present for each element in order from most to least abundant (* denoting radioisotopes), and the specific activity for each alloy.

	CCZ		CCNZ		
Solute	Non-irradiated composition (wt%)	Post-irradiation composition (wt%)	Non-irradiated composition (wt%)	Post-irradiation composition (wt%)	Isotopes present
Cu	99.12	97.0762	96.5	94.511725	^{63}Cu and ^{65}Cu
Cr	0.81	0.807206	2	1.9933811	^{52}Cr, ^{53}Cr, ^{50}Cr, and ^{54}Cr
Nb			1.35	1.34779815	^{93}Nb, ^{94}Nb*, ^{93m}Nb*, and ^{92}Nb*
Zr	0.07	0.071968	0.15	0.14994391	^{90}Zr, ^{94}Zr, ^{92}Zr, ^{91}Zr, ^{96}Zr*, and ^{93}Zr*
Ni		1.01786		0.99073538	^{64}Ni, ^{63}Ni*, ^{62}Ni, ^{60}Ni, and ^{61}Ni
Zn		1.023877		0.99697277	^{64}Zn, ^{66}Zn, ^{67}Zn, ^{65}Zn*, and ^{68}Zn
Co		1.71E-05		1.6633E-05	^{60}Co* and ^{59}Co
V		0.002779		0.00686044	^{51}V and ^{50}V*
Mo		1.77E-05		0.00241366	^{95}Mo, ^{96}Mo, and ^{94}Mo, ^{97}Mo and ^{98}Mo
H		2.86E-05		2.7756E-05	^{1}H
Mn		4.63E-05		0.00011423	^{55}Mn
	Specific activity: 4.33 mCi/g		Specific activity: 6.20 mCi/g		

3.3 Transmutation products

Transmutation calculations performed using the ORIGEN code found that for both the CCZ and CCNZ alloys at T_{ir} = 300°C, roughly 1wt% Ni and 1wt% Zn were expected to form through the transmutation of Cu (Table 2). The higher starting composition of Cu in CCZ results in slightly more production of each solute (1.02wt % vs. 0.99wt%). The only significant departure from CCZ in the CCNZ transmutation products is the addition of Mo, a transmutation product of Nb. The overall specific activity of the CCNZ alloys (6.20 mCi/g) is roughly 50% higher than CCZ alloys (4.33 mGi/g) for a decay time of roughly 3 years post-irradiation due to the presence of long half-life Nb radioisotopes.

3.4 Microstructure

The microstructure of the corresponding non-irradiated, as-aged CCNZ alloy was composed of a Cr_2Nb Laves phase with an average size of 2–11 μm at grain boundaries, nanoscale Cr precipitates with an average size of 5 nm, and a bimodal grain size distribution of ~22 μm and ~104 μm grains in the Cu matrix, with an overall average grain size of ~40 μm (Wang et al., 2020). In the non-irradiated CCNZ alloys, cracking during deformation was observed to be less severe at grain boundaries which contained the Cr_2Nb phase. SEM characterization of irradiated samples found that the Cr_2Nb Laves phase was retained and showed little change in size and morphology from the non-irradiated CCNZ. Likewise, the bimodal grain size distribution observed in as-aged CCNZ was retained after irradiation, which can broadly be observed at lower magnifications (Figure 4A). However, significant pore/void formation at the micron scale in narrow regions at Laves boundaries is observed in the irradiated, undeformed microstructure (Figures 4A, B). The total area fraction of the voids is estimated to be 0.36% ± 0.12%. These voids may be the result of H and He bubble and vacancy coalescence at interfaces and could operate as crack initiation sites during tensile testing. In deformed regions on tensile specimens, cracking was also observed in the Laves phase which was not connected to porous regions (Figure 4C) and was not observed in the non-irradiated CCNZ alloys. This suggests that the Laves phase is embrittled during irradiation. Some Cr nanoprecipitates are visible in high-mag SEM images from specimens at all irradiation temperatures, with some seen to be roughly ~200 nm in diameter, indicating precipitate growth during irradiation (Figure 4C).

Energy dispersive X-ray spectroscopy (EDS) was used to estimate relative concentrations of each element in the irradiated microstructures; while the standard error in EDS measurements is 1–2 at%, limiting its usefulness in quantifying low concentration elements, the relative concentrations of elements can be used to assess changes in concentrations across irradiation conditions. Characterization of irradiated CCNZ at three irradiation temperatures found that the ratio of transmutation products Ni and Zn in the matrix at T_{ir} = 254°C (Figure 5) was larger than at high

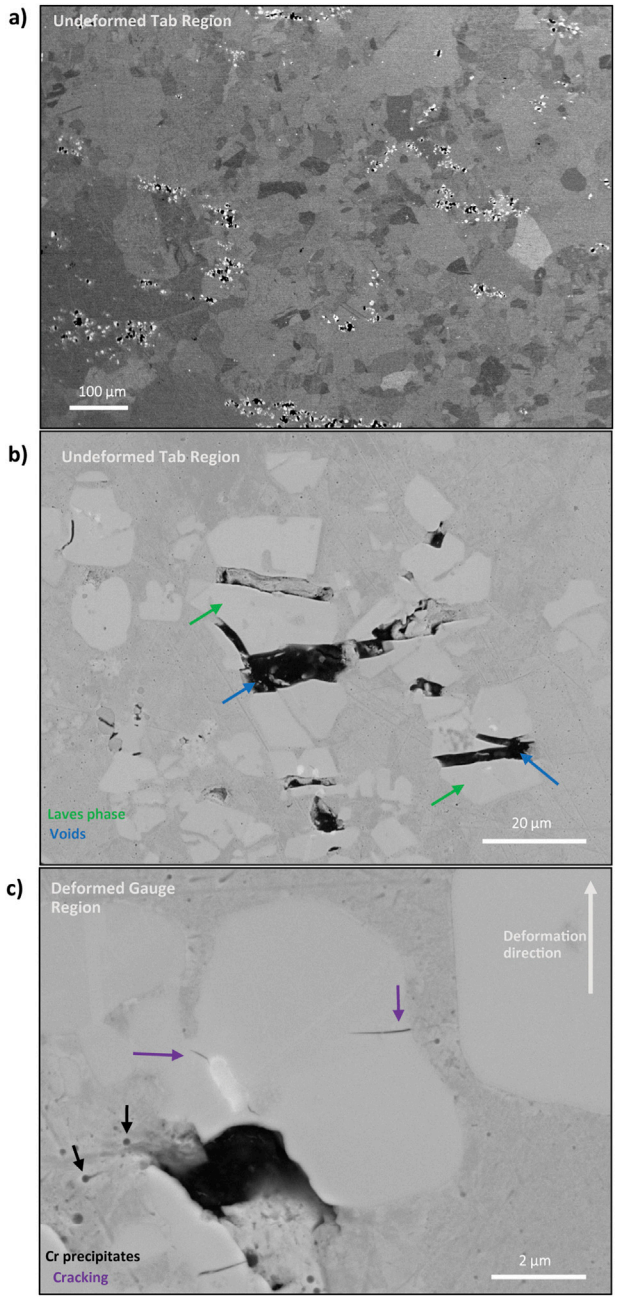

FIGURE 4
(A) Low-mag microstructure of undeformed CCNZ (T_{ir} = 318°C) showing pore/void formation around Laves phase (whitish phase) and high-contrast grains. **(B)** Microstructure of voids around the Laves phase in undeformed CCNZ. **(C)** Microstructure of deformed CCNZ showing crack initiation in the Laves phase (outlined in green).

temperatures (i.e., the relative amount of Ni in the matrix decreased with increasing irradiation temperatures). A higher Zr concentration was also detected in the Cu matrix at lower irradiation temperatures than higher temperatures.

APT was performed to obtain exact compositions of each phase in CCNZ on the sample with T_{ir} = 318°C: the Cu matrix, the Cr_2Nb Laves phase, and the Cr precipitates dispersed throughout the matrix (Table 3), which allowed for quantification of the exact levels of solute in the Cu matrix and dispersion of transmutation products. The primary transmutation products measured in the Cr_2Nb Laves phase were V and Co, which may contribute to the observed phase embrittlement. At this temperature, very low concentrations of Zr were detected in the matrix (0.01 at%); instead, the bulk of the Zr present was observed to segregate to the Cr precipitates (1.35 at%), along with significant concentrations of Ni (11.45 at%) (Figure 6). The remaining Ni concentration in the matrix is 1.12 at%, along with a concentration of Zn at 1.77 at%, comprising the vast majority of the Zn present. APT also found that the average Cr precipitate diameter at that scale was 2 nm, slightly finer than the 5 nm diameter observed in non-irradiated CCNZ. The appearance of both finer (2 nm) and coarser (200 nm) Cr precipitates in the irradiated microstructure can be attributed to multiple competing effects. Partial ballistic dissolution of the Cr precipitates dissolved Cr into solid solution, while some of this Cr was recombined through radiation-induced precipitation to produce finer Cr nanoprecipitates; thermal diffusion of Cr increases with temperature (Nelson et al., 1972; Zhao et al., 2022).

4 Discussion

Previous research on neutron irradiated copper and CCZ alloys has found that significant radiation hardening (mainly associated with formation of nanoscale stacking fault tetrahedra (SFT) and dislocation loops) occurs for irradiation temperatures up to ~275 °C, whereas slight softening in CCZ has been reported for irradiation temperatures >275 °C due to reduced SFT and loop formation along with potential precipitate coarsening (Li and Zinkle, 2020; Barabash et al., 2011; Zinkle and Fabritsiev, 1994; Fenici et al., 1994; Fabritsiev et al., 2004; Fabritsiev et al., 1996). Irradiation generally causes an increase in electrical resistivity due to increased electron scattering from transmutant solutes and radiation-induced defect clusters (SFTs, loops, cavities) (Chaplin and Coltman, 1982; Li and Zinkle, 2020; Zinkle and Fabritsiev, 1994; Fabritsiev et al., 1996; Fabritsiev and Pokrovsky, 2005; Edwards et al., 2007; Frost and Kennedy, 1986; Singh et al., 1997; Edward et al., 1994; Fabritsiev et al., 1998; Fabritsiev and Pokrovsky, 1997). The electrical resistivity increase associated with the creation of nanoscale defect clusters (SFTs, loops) during the irradiation of Cu near room temperature saturates after ~0.1 dpa at a value of ~0.1 μΩ-cm and therefore only contributes in a minor way to the observed electrical resistivity changes for the current irradiation conditions (Chaplin and Coltman, 1982; Birtcher and Blewitt, 1981).

Multiple temperature-sensitive competing effects in the changing microstructure may operate during irradiation, such as ballistic mixing and dissolution of precipitates, solute diffusion, transmutation, and defect formation. These can contribute to changes in the strengthening contributions from precipitates, solute in solid solution, and defect formation. The detection of higher levels of Ni and Zr in the matrix at lower irradiation temperatures is likely due to the dominance of ballistic mixing at lower temperatures compared to thermal diffusion (Nelson et al., 1972; Zhao et al., 2022). The resulting solid solution strengthening from Ni and Zr at lower temperatures may partly explain why greater radiation hardening is observed at lower temperatures. Although changes to the volume fraction and particle size of the

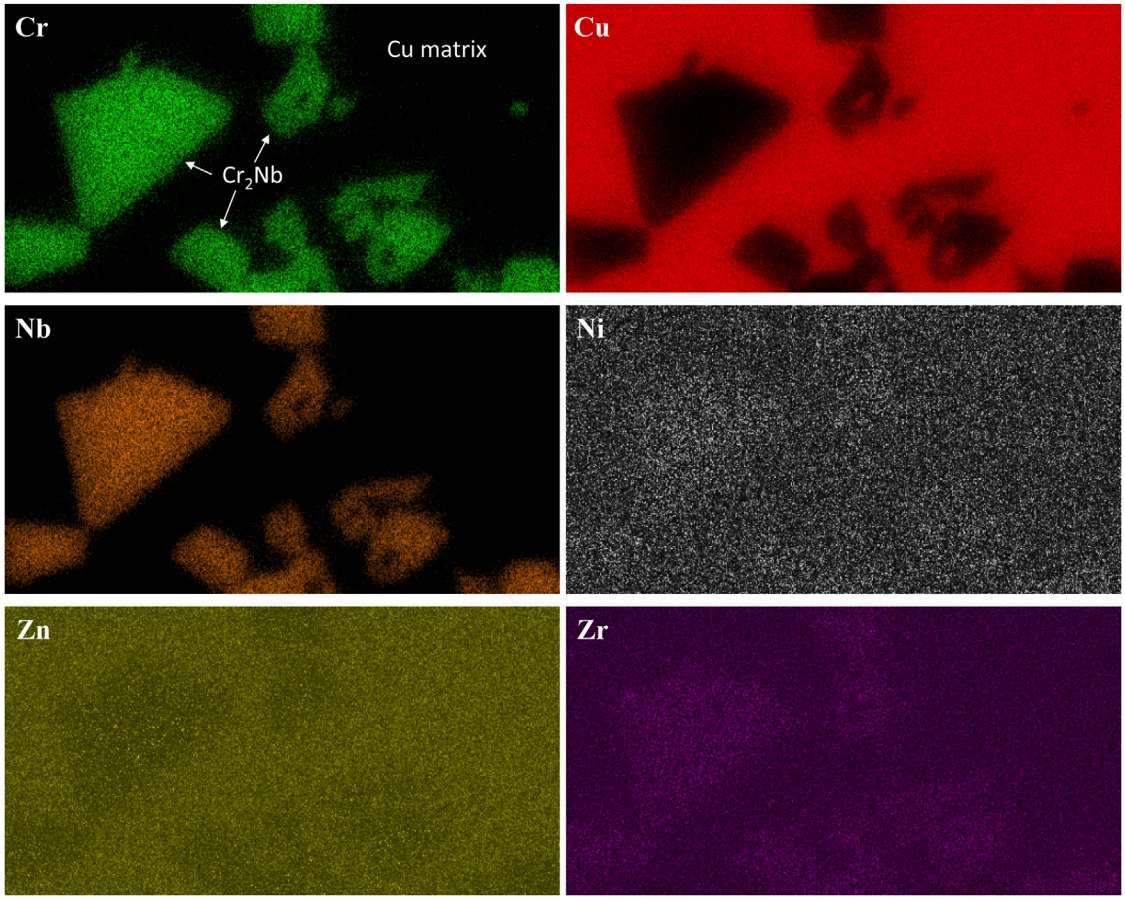

FIGURE 5
EDS composition maps of undeformed CCNZ (T_{ir} = 250 °C) showing concentrations of each element in the matrix and Laves phases (contrast enhanced for low-concentration elements Ni, Zn, and Zr).

TABLE 3 Compositions of matrix, Cr_2Nb_2, and Cr precipitates calculated from APT data.

Element phase	Cu	Cr	Nb	Zr	Ni	Zn	V	Co	Fe
Matrix (at%)	97.03	0.04	0	0.01	1.12	1.77	0	0.002	0.02
Cr_2Nb (at%)	1.26	62.80	35.28	0.002	0.03	0.01	0.30	0.21	0.05
Cr precipitates (at%)	26.89	59.45	0	1.35	11.45	0.42	0.45	0	0

Laves phase were not observed, defect consolidation around the Laves phase and the observed embrittlement of the Laves phase affected its efficacy for strengthening. Likewise, the competing effect of solid solution strengthening in the Cu matrix may have improved the yield strength. The introduction of nanoscale SFT and dislocation loop defect clusters that can be sheared by gliding dislocations, also with embrittlement of the Laves phase and void formation at Laves/matrix interfaces, are likely the primary contributors to the observed drop in elongation. The greater levels of solute in the matrix at lower temperatures is also likely a contributing factor to the higher electrical resistivity of the CCNZ samples irradiated at lower temperatures, peaking at 4.47 μΩ·cm at 268 °C (an increase of 87%) compared to the 55% increase to 3.7 μΩ·cm observed at 294 °C.

The detailed local concentration and distribution data obtained from APT provides total levels of solute in solid solution in the Cu matrix for the sample irradiated at 318 °C. The effect of each of these solutes in solid solution on the conductivity of pure Cu is well-documented in the literature (Davis and ASM International, 2001; MaterialsAmerican Society for Testing, 1991; Simon et al., 1992). Table 4 summarizes the resistivity increase per 1wt% increase, the wt% of that solute in the irradiated alloy matrix (calculated by ORIGEN), and the corresponding calculated net resistivity increase caused by each solute in this system. These values assume a linear increase in resistivity with solute additions, which is only a valid assumption for small additions of each solute and when the distance between impurities is large (Žnidarič, 2022). The concentrations of each

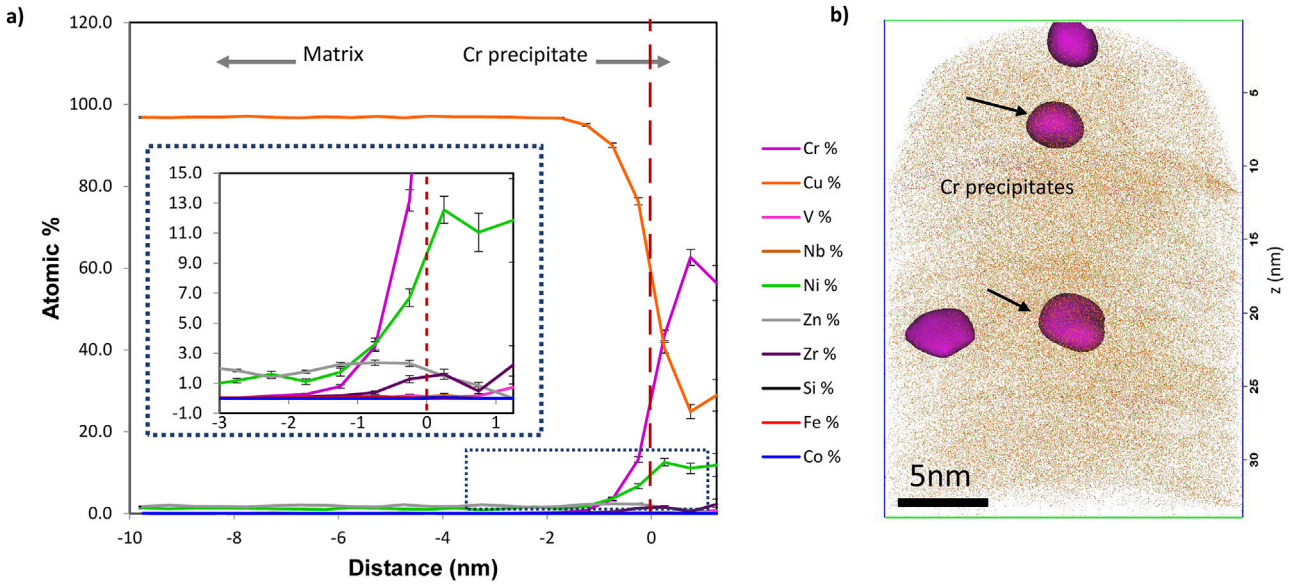

FIGURE 6
(A) Atom probe tomography composition data for the matrix–Cr precipitate interface showing Ni and Zr enrichment in precipitates. **(B)** APT needle reconstruction with Cr isosurfaces representing precipitates.

TABLE 4 Net contributions of solutes in solid solution to Cu alloy resistivity (MaterialsAmerican Society for Testing, 1991; Davis and ASM International, 2001; Simon et al., 1992). Although contributions from Cr are included, its concentration in the matrix is within solubility limits in Cu at the aging temperature, suggesting that Cr contributions have not changed due to irradiation.

Solute	Resistivity increase per 1wt% (μΩ-cm)	Concentration in Cu matrix (wt%) (%)	Approximate $\Delta\rho_{net}$ contribution (μΩ-cm)
Co	7.3	0.002	0.01
Cr*	4.9	0.034	0.17
Fe	10.6	0.019	0.20
Ni	1.2	1.039	1.25
Si	7.0	0.001	0.01
Zn	0.286	1.824	0.52
Zr	8.0	0.011	0.09
Total			**2.25**
Total excluding Cr			**2.08**

Therefore, a total including and excluding contributions from Cr is included in the table (bolded values).

solute observed are near or below their individual solubility limits in Cu (MaterialsAmerican Society for Testing, 1991) and can reasonably be considered within this linear regime. With these values, the contributions from each solute can be added according to Matthiessen's rule, which states that the total resistivity of a metal is the sum of contributions due to imperfections in the crystal as well as thermal vibrations of the lattice. Although the net contributions for each solute total 2.08 μΩ·cm are based on the composition of the Cu matrix (Table 4), the experimental change in resistivity, $\Delta\rho_{exp}$, for CCNZ alloys only amounts to 1.55 μΩ·cm. The overestimation from individual solute contributions is likely due to a lack of published data on the mechanisms by which the non-irradiated sample's resistivity is increased from pure Cu, and due to any non-linearity in solute contributions. However, it is still useful to use the known solute data for these alloys to assess the relative importance of different irradiation effects on the change in resistivity, such as transmutation, ballistic mixing, and radiation- or thermally induced segregation and partitioning.

The total change in the resistivity of each alloy, $\Delta\rho$, after irradiation can be broken down into several contributions:

$$\Delta\rho = \Delta\rho_{tr} + \Delta\rho_{bal} + \Delta\rho_{ssp} + \Delta\rho_{def}, \quad (3)$$

where $\Delta\rho_{tr}$ is the total change in resistivity due to transmutation products in solid solution in the matrix phase, $\Delta\rho_{bal}$ is the resistivity

change due to ballistic mixing of Zr and Cr precipitates back into the matrix (into solid solution), $\Delta\rho_{sp}$ is the change in resistivity due to solute partitioning (original solutes or transmutation products) to precipitates or nanoscale voids, and $\Delta\rho_{def}$ is the contribution from nanoscale defect clusters and dislocation loops. Although microstructural features such as grain boundaries can impact electrical resistivity, the similarity of the Laves phase size and morphology, as well as the grain sizes and grain size distribution, between irradiated and unirradiated CCNZ suggests that this contribution remains relatively constant during irradiation.

To quantify the effect of solute partitioning, maximum possible contributions of each solute are calculated in the case of zero partitioning to precipitates. Maximum contributions from ballistic mixing ($\Delta\rho_{bal\_total}$) will comprise the contributions from Cr and Zr in matrix, with the assumption that the non-irradiated matrix content of each is at the solubility limit for the aging temperature of CCNZ, 475 °C, which is 0.0wt% for Zr and 0.045wt% for Cr (Kang and Jung, 2010; Alexander, 1939). It also requires consideration of the maximum possible concentration of Zr in the matrix in the case of no Zr partitioning to Cr precipitates (Zr = 0.15 wt% in this case). Because Cr in the irradiated matrix is below this limit, the ballistic contributions from Cr solute are 0, while $\Delta\rho_{bal\_Zr} = 1.2\mu\Omega \cdot \text{cm}$. A maximum contribution from transmutation ($\Delta\rho_{tr\_total}$) will assume that all transmutation products which originated in the Cu matrix have stayed in the matrix—that is, Ni and Zn are both present in equal amounts, up to 1.824wt%—resulting in contributions of $\Delta\rho_{tr\_Zn} = 0.52\mu\Omega \cdot \text{cm}$ and $\Delta\rho_{tr\_Ni} = 2.19\mu\Omega \cdot \text{cm}$ and also including minor contributions from transmutant solutes Co, Fe, and Si. Contributions from solute partitioning ($\Delta\rho_{sp\_total}$) of Ni and Zr, then, will be negative, as this considers the difference in the experimental matrix composition, and these maximum concentrations used in calculating ballistic and transmutation contributions. $\Delta\rho_{sp\_Ni} = -0.94\mu\Omega \cdot \text{cm}$ and $\Delta\rho_{sp\_Zr} = -1.11\mu\Omega \cdot \text{cm}$. Additionally, as the concentration of Cr in the matrix (0.034wt%) is lower than the aging temperature solubility, we can consider the depletion of Cr from the matrix through re-precipitation under the contribution $\Delta\rho_{sp\_Cr} = -0.05\mu\Omega \cdot \text{cm}$. Under these assumptions,

$$\Delta\rho_{tr\_total} = 2.94\,\mu\Omega \cdot \text{cm}$$
$$\Delta\rho_{bal\_total} = 1.2\,\mu\Omega \cdot \text{cm}$$
$$\Delta\rho_{sp\_total} = -2.1\,\mu\Omega \cdot \text{cm}.$$

When these contributions are used to calculate [$\Delta\rho_{total}$] in Equation 3, they sum approximately to the original predicted change from solutes (as each calculation introduced rounding error), $\Delta\rho_{total} = 2.04\ \mu\Omega\cdot\text{cm}$. For the moderate-dose (~5 dpa) irradiation conditions being investigated, defect clusters make a relatively minor contribution to resistivity ($\Delta\rho_{def}$ ~0.1 μΩ·cm) compared with the solute-relevant effects (Chaplin and Coltman, 1982; Birtcher and Blewitt, 1981). Comparison of these contributions finds that the primary influence on the resistivity in these alloys will be transmutation, followed by solute partitioning to precipitates, ballistic mixing, and then defect clusters. These results highlight the importance of a high-volume density of Cr precipitates in the matrix, not only for strengthening but as a means of mitigating resistivity change under irradiation by providing preferential segregation sites for Ni and Zr solutes, depleting their matrix concentrations; this is more effective at higher temperatures when greater thermal diffusion rates will increase their mobility through the matrix.

Although the presence of Nb is prohibitive for fusion energy systems in terms of acceptable activity limits even in scant quantities (Fetter et al, 1988), the enhanced creep rupture life afforded by the addition of the Laves phase is an attractive design feature of the CCNZ alloys given the relatively similar post-irradiation tensile and electrical properties of CCNZ and CCZ. We suggest that redesign with a different Laves-forming solute could be a promising design strategy for the future development of commercially viable creep-resistant Cu alloys for nuclear fusion.

5 Conclusion

Cu–Cr–Nb–Zr (CCNZ) alloys designed to improve the creep resistance of ITER-grade Cu–Cr–Zr (CCZ) alloys were neutron irradiated to 5dpa at 250–325 °C. Post-irradiation experiments found radiation hardening to be more significant in CCNZ (36% increase at 250 °C) than CCZ (17% increase at 250 °C), but the trend of a decrease in hardening with increasing irradiation temperature was observed for both. The ultimate tensile strength of irradiated CCNZ was found to be similar to non-irradiated CCNZ and remained relatively stable with increasing T_{ir}—within 10% of non-irradiated values—but the yield strength, elongation, hardness, and electrical resistivity data all suggest the influence of competing factors such as solute partitioning and transmutation which have temperature-dependent influence. Evidence for embrittlement in the Cr_2Nb Laves phase and pore formation at the matrix–Laves interfaces were the most significant microstructure changes observed. Transmutation calculations found that CCNZ and CCZ alloys both produced ~1wt% each of Ni and Zn through Cu transmutation, and these products were the most significant contributors to the increase in electrical resistivity. APT revealed substantial partitioning of Zr and Ni to the nanoscale Cr precipitates, reducing the resistivity contributions of each solute. These results suggest that the addition of a Laves phase is a promising design concept for improving the creep properties of CCZ alloys for fusion environments without severely compromising electrical and thermal conductivity.

Licenses and Permissions

Data availability statement

The original contributions presented in the study are included in the article/supplementary material; further inquiries can be directed to the corresponding author.

Author contributions

AP: data curation, formal analysis, investigation, writing–original draft, and writing–review and editing. DH: data curation, formal analysis, investigation, and writing–review and editing. JG: project administration, resources, supervision, and writing–review and editing. SZ: conceptualization, funding acquisition, project administration, resources, and writing–review and editing. YY: conceptualization, formal analysis, funding acquisition, resources, supervision, writing–original draft, and writing–review and editing. SS: data curation, formal analysis, investigation, and writing–review and editing. JP: data curation, investigation, visualization, and writing–review and editing. YK: conceptualization, funding acquisition, project administration, resources, supervision, and writing–review and editing.

Funding

The authors declare that financial support was received for the research, authorship, and/or publication of this article. Research was sponsored by the Office of Fusion Energy Sciences and U.S. Department of Energy under contract DE-AC05-00OR22725 with UT-Battelle LLC. The Laboratory Directed Research and Development Program of Oak Ridge National Laboratory funded part of the microscopy, formal analysis, and writing and editing of this manuscript.

Acknowledgments

The authors thank Travis Dixon for the preparation of SEM samples, Kyle Everett for data acquisition of hardness and tensile properties, Amy Godfrey for measurements of electrical resistivity, and Tim Lach for assistance in APT needle preparation. This research used resources at the High Flux Isotope Reactor (HFIR) and the Center for Nanophase Materials Sciences (CNMS) for sample irradiation and APT measurements, which are both DOE Office of Science User Facilities operated by Oak Ridge National Laboratory.

Conflict of interest

The authors declare that the research was conducted in the absence of any commercial or financial relationships that could be construed as a potential conflict of interest.

Publisher's note

References

Alexander, W. O. (1939). Annealing characteristics and solid solubility limits of copper and copper alloys containing chromium. *J. Inst. Metals* 64, 93–113.

Anderson, K. R., Groza, J. R., Dreshfield, R. L., and Ellis, D. (1995). High-performance dispersion-strengthened Cu-8 Cr-4 Nb alloy. *Metallurgical Mater. Trans. A* 26 (9), 2197–2206. doi:10.1007/BF02671235

Asakura, N., Hoshino, K., Kakudate, S., Subba, F., You, J.-H., Wiesen, S., et al. (2023). Recent progress of plasma exhaust concepts and divertor designs for tokamak DEMO reactors. *Nucl. Mater. Energy* 35, 101446. doi:10.1016/j.nme.2023.101446

Bahl, S., Sisco, K., Yang, Y., Theska, F., Primig, S., Allard, L. F., et al. (2021). Al-Cu-Ce(-Zr) alloys with an exceptional combination of additive processability and mechanical properties. *Addit. Manuf.* 48 (December), 102404. doi:10.1016/j.addma.2021.102404

Barabash, V., Peacock, A., Fabritsiev, S., Kalinin, G., Zinkle, S., Rowcliffe, A., et al. (2007). Materials challenges for ITER – current status and future activities. *J. Nucl. Mater.* 367–370, 21–32. doi:10.1016/j.jnucmat.2007.03.017

Barabash, V. R., Kalinin, G. M., Fabritsiev, S. A., and Zinkle, S. J. (2011). Specification of CuCrZr alloy properties after various thermo-mechanical treatments and design allowables including neutron irradiation effects. *J. Nucl. Mater.* 417 (1–3), 904–907. doi:10.1016/j.jnucmat.2010.12.158

Birtcher, R. C., and Blewitt, T. H. (1981). Damage saturation effects on volume and resistivity changes induced by fission-fragment irradiation of copper. *J. Nucl. Mater.* 98 (1–2), 63–70. doi:10.1016/0022-3115(81)90387-1

Campbell, A. A., Porter, W. D., Katoh, Y., and Snead, L. L. (2016). Method for analyzing passive silicon carbide thermometry with a continuous dilatometer to determine irradiation temperature. *Nucl. Instrum. Methods Phys. Res. Sect. B Beam Interact. Mater. Atoms* 370, 49–58. doi:10.1016/j.nimb.2016.01.005

Chaplin, R. L., and Coltman, R. R. (1982). Defects and transmutations in reactor-irradiated copper. *J. Nucl. Mater.* 108–109, 175–182. doi:10.1016/0022-3115(82)90485-8

Cheng, B., Wang, L., Sprouster, D. J., Trelewicz, J. R., Zhong, W., Yang, Y., et al. (2021). Tailoring microstructure in sintered Cu-Cr-Nb-Zr alloys for fusion components. *J. Nucl. Mater.* 551 (August), 152956. doi:10.1016/j.jnucmat.2021.152956

Davis, J. R., and ASM International (2001). in Copper and copper alloys. *ASM specialty handbook* (Materials Park, OH: ASM International).

Echols, J. R., Garrison, L. M., Reid, N., Parish, C. M., Hasegawa, A., Bhattacharya, A., et al. (2023). Degradation of electrical resistivity of tungsten following shielded neutron irradiation. *Acta Mater.* 257 (September), 119025. doi:10.1016/j.actamat.2023.119025

Edwards, D. J., Garner, F. A., and Greenwood, L. R. (1994). The influence of transmutation, void swelling, and flux/spectra uncertainties on the electrical properties of copper and copper alloys. *J. Nucl. Mater.* 212–215, 404–409. doi:10.1016/0022-3115(94)90094-9

Edwards, D. J., Singh, B. N., and Tähtinen, S. (2007). Effect of heat treatments on precipitate microstructure and mechanical properties of a CuCrZr alloy. *J. Nucl. Mater.* 367–370, 904–909. doi:10.1016/j.jnucmat.2007.03.064

EUROfusion (2024). The demonstration power plant: DEMO. *EUROfusion Realiz. Fusion Energy*. Available at: https://euro-fusion.org/programme/demo/(Accessed October 3, 2024).

Fabritsiev, S. A., and Pokrovsky, A. S. (1997). The effect of neutron irradiation on the electrical resistivity of high-strength copper alloys. *J. Nucl. Mater.* 249 (2–3), 239–249. doi:10.1016/S0022-3115(97)00144-X

Fabritsiev, S. A., and Pokrovsky, A. S. (2005). Effect of high doses of neutron irradiation on physico-mechanical properties of copper alloys for ITER applications. *Fusion Eng. Des.* 73 (1), 19–34. doi:10.1016/j.fusengdes.2004.12.003

Fabritsiev, S. A., and Pokrovsky, A. S. (2007). Effect of irradiation temperature on microstructure, radiation hardening and embrittlement of pure copper and copper-based alloy. *J. Nucl. Mater.* 367–370, 977–983. doi:10.1016/j.jnucmat.2007.03.056

Fabritsiev, S. A., Pokrovsky, A. S., and Ostrovsky, S. E. (2004). Effect of the irradiation–annealing–irradiation cycle on the mechanical properties of pure copper and copper alloy. *J. Nucl. Mater.* 324 (1), 23–32. doi:10.1016/j.jnucmat.2003.09.004

Fabritsiev, S. A., Pokrovsky, A. S., and Zinkle, S. J. (1998). Effect of neutron dose and spectra, He/dpa ratio and Ni and Zn accumulation on irradiation damage of pure copper and PH and DS copper alloys. *Fusion Eng. Des.* 38 (4), 459–473. doi:10.1016/S0920-3796(98)00106-9

Fabritsiev, S. A., Zinkle, S. J., and Singh, B. N. (1996). Evaluation of copper alloys for fusion reactor divertor and first wall components. *J. Nucl. Mater.* 233–237, 127–137. doi:10.1016/S0022-3115(96)00091-8

Fenici, P., Boerman, D. J., Tartaglia, G. P., and Elen, J. D. (1994). Effect of fast-neutron irradiation on tensile properties of precipitation-hardened Cu-Cr-Zr alloy. *J. Nucl. Mater.* 212–215, 399–403. doi:10.1016/0022-3115(94)90093-0

Fetter, S., Cheng, E. T., and Mann, F. M. (1988). Long-term radioactivity in fusion reactors. *Fusion Eng. Des.* 6, 123–130. doi:10.1016/S0920-3796(88)80098-X

Field, K. G., McDuffee, J. L., Geringer, J. W., Petrie, C. M., and Katoh, Y. (2019). Evaluation of the continuous dilatometer method of silicon carbide thermometry for passive irradiation temperature determination. *Nucl. Instrum. Methods Phys. Res. Sect. B Beam Interact. Mater. Atoms* 445, 46–56. doi:10.1016/j.nimb.2019.02.022

Frost, H. M., and Kennedy, J. C. (1986). Porosity swelling and transmutation contributions to conductivity changes in some neutron-irradiated copper alloys. *J. Nucl. Mater.* 141–143, 169–173. doi:10.1016/S0022-3115(86)80030-7

Groh, H. C., Ellis, D., and Loewenthal, W. (2008). Comparison of GRCop-84 to other Cu alloys with high thermal conductivities. *J. Mater. Eng. Perform.* 17, 594–606. doi:10.1007/s11665-007-9175-3

Gusarov, A., Pohl, C., Pfalz, T., Bosch, R.-W., Van Dyck, S., Barabash, V., et al. (2018). Assessment of creep in reactor-irradiated CuCrZr alloy intended for the ITER first wall panels. *Fusion Eng. Des.* 137, 112–123. doi:10.1016/j.fusengdes.2018.09.001

Howard, R. H., and Smith, K. R. (2018). *Development of a flexible design for irradiation of miniature tensile and charpy test specimens in the high flux isotope reactor*. United States: TM-2018/872. Oak Ridge National Laboratory. Available at: https://www.osti.gov/.

ITER Organization (2024). A few lines. *ITER*. Available at: https://www.iter.org/proj/inafewlines (Accessed October 3, 2024).

Kalinin, G. M., Artyugin, A. S., Yvseev, M. V., Shushlebin, V. V., Sinelnikov, L. P., and Strebkov, Yu.S. (2011). The effect of irradiation on tensile properties and fracture toughness of CuCrZr and CuCrNiSi alloys. *J. Nucl. Mater.* 417 (1–3), 908–911. doi:10.1016/j.jnucmat.2011.02.036

Kang, D. H., and Jung, I.-Ho (2010). Critical thermodynamic evaluation and optimization of the Ag–Zr, Cu–Zr and Ag–Cu–Zr systems and its applications to amorphous Cu–Zr–Ag alloys. *Intermetallics* 18 (5), 815–833. doi:10.1016/j.intermet.2009.12.013

Krishna, S. C., Muneshwar, P., Pant, B., and Korla, R. (2022). Hot deformation behavior and processing map of Cu-Cr-Nb-Zr alloy. *J. Mater. Eng. Perform.* 31 (2), 1325–1337. doi:10.1007/s11665-021-06268-0

Li, M., and Zinkle, S. J. (2020). "Physical and mechanical properties of copper and copper alloys," in *Comprehensive nuclear materials*. 2nd ed. (Oxford: Elsevier), 6, 667–690. doi:10.1016/B978-0-08-056033-5.00122-1

Materials, American Society for Testing (1991). *Annual book of ASTM standards*. ASTM, University of California, c1970–c2001.

Nelson, R. S., Hudson, J. A., and Mazey, D. J. (1972). The stability of precipitates in an irradiation environment. *J. Nucl. Mater.* 44 (3), 318–330. doi:10.1016/0022-3115(72)90043-8

Siccinio, M., Biel, W., Cavedon, M., Fable, E., Federici, G., Janky, F., et al. (2020). DEMO physics challenges beyond ITER. *Fusion Eng. Des.* 156 (July), 111603. doi:10.1016/j.fusengdes.2020.111603

Simon, N. J., Drexler, E. S., and Reed, R. P. (1992). "Properties of copper and copper alloys at cryogenic temperatures," in *Nist mono* (Gaithersburg, MD: National Institute of Standards and Technology). doi:10.6028/NIST.MONO.177

Singh, B. N., Edwards, D. J., Eldrup, M., and Toft, P. (1997). Effects of heat treatments and neutron irradiation on microstructures and physical and mechanical properties of copper alloys. *J. Nucl. Mater.* 249 (1), 1–16. doi:10.1016/S0022-3115(97)00184-0

Skutnik, S. E., and Austin, C. S. (2023). High flux isotope reactor neutron spectrum shape estimation from activation experiment data. *IEEE Trans. Nucl. Sci.* 70 (1), 44–57. doi:10.1109/TNS.2022.3226870

Terentyev, D., Rieth, M., Pintsuk, G., Von Müller, A., Antusch, S., Zinovev, A., et al. (2023). Effect of neutron irradiation on tensile properties of advanced Cu-based alloys and composites developed for fusion applications. *J. Nucl. Mater.* 584, 154587. doi:10.1016/j.jnucmat.2023.154587

Wang, H.-S., Chen, H.-G., Gu, J.-W., Hsu, C.-En, and Wu, C.-Y. (2015). Improvement in strength and thermal conductivity of powder metallurgy produced Cu–Ni–Si–Cr alloy by adjusting Ni/Si weight ratio and hot forging. *J. Alloys Compd.* 633, 59–64. doi:10.1016/j.jallcom.2015.02.024

Wang, L., Zheng, Ce, Kombaiah, B., Tan, L., Sprouster, D. J., Snead, L. L., et al. (2020). Contrasting roles of Laves_Cr2Nb precipitates on the creep properties of novel CuCrNbZr alloys. *Mater. Sci. Eng. A* 779 (March), 139110. doi:10.1016/j.msea.2020.139110

Wieselquist, W., and Lefebvre, R. (2023). *SCALE 6.3.1 user manual*. ORNL/TM-SCALE-6.3.1, 1959594, ORNL/TM-SCALE-6.3.1. doi:10.2172/1959594

Xoubi, N., and Primm, R. T. (2004). *Modeling of the high flux isotope reactor cycle 400*. United States: TM-2004/251. Oak Ridge National Laboratory. Available at: https://www.osti.gov/.

Yang, Y., Wang, L., Snead, L., and Zinkle, S. J. (2018). Development of novel Cu-Cr-Nb-Zr alloys with the aid of computational thermodynamics. *Mater. and Des.* 156, 370–380. doi:10.1016/j.matdes.2018.07.003

You, J.-Ha (2015). Copper matrix composites as heat sink materials for water-cooled divertor target. *Nucl. Mater. Energy* 5, 7–18. doi:10.1016/j.nme.2015.10.001

You, J. H., Visca, E., Barrett, T., Böswirth, B., Crescenzi, F., Domptail, F., et al. (2021). High-heat-flux technologies for the European demo divertor targets: state-of-the-art and a review of the latest testing campaign. *J. Nucl. Mater.* 544, 152670. doi:10.1016/j.jnucmat.2020.152670

Zhao, Y., Bhattacharya, A., Pareige, C., Massey, C., Zhu, P., Poplawsky, J. D., et al. (2022). Effect of heavy ion irradiation dose rate and temperature on α' precipitation in high purity Fe-18%Cr alloy. *Acta Mater.* 231 (117888), 117888. doi:10.1016/j.actamat.2022.117888

Zinkle, S. J. (2014). Evaluation of high strength, high conductivity CuNiBe alloys for fusion energy applications. *J. Nucl. Mater.* 449 (1–3), 277–289. doi:10.1016/j.jnucmat.2013.09.007

Zinkle, S. J. (2016). Applicability of copper alloys for DEMO high heat flux components. *Phys. Scr.* T167, 014004. doi:10.1088/0031-8949/2015/T167/014004

Zinkle, S. J., and Fabritsiev, S. A. (1994). "Copper alloys for high heat flux structure applications," in *International atomic energy agency, Vienna (Austria); nuclear fusion*, 268, 163–192.

Zinkle, S. J., and Ghoniem, N. M. (2000). Operating temperature windows for fusion reactor structural materials. *Fusion Eng. Des.* 51–52, 55–71. doi:10.1016/S0920-3796(00)00320-3

Žnidarič, M. (2022). Modified Matthiessen's rule: more scattering leads to less resistance. *Phys. Rev. B* 105 (4), 045140. doi:10.1103/PhysRevB.105.045140